Coupling between finite volume method and lattice Boltzmann method and its application to fluid flow and mass transport in proton exchange membrane fuel cell

Li Chen, Huibao Luan, Yongliang Feng, Chenxi Song, Ya-Ling He, Wen-Quan Tao *

Key Laboratory of Thermo-Fluid Science and Engineering of MOE, School of Energy and Power Engineering, Xi'an Jiaotong University, Xi'an, Shaanxi 710049, China

ARTICLE INFO

ABSTRACT

In this paper, a concentration distribution function reconstruction operator is derived to lift macroscopic parameter concentration to concentration distribution function in lattice Boltzmann method (LBM). Combined with a density–velocity distribution function reconstruction operator previously derived by the author's group, the coupled finite volume method and LBM scheme (CFVLBM), previously proposed by the authors' group is extended to simulate both fluid flow and mass transport processes. The accuracy of concentration distribution function reconstruction operator and the feasibility of CFVLBM are validated by two numerical examples, diffusion–convection–reaction problem and natural convection in a square cavity induced by concentration gradient. Finally, the CFVLBM is further adopted to simulate fluid flow and mass transport in the gas channel (GC) and gas diffusion layer (GDL) of a proton exchange membrane fuel cell (PEMFC). It is found that the CFVLBM can capture the pore-scale information of fluid flow and species transport in porous GDL and can save the computational resources.

© 2012 Elsevier Ltd. All rights reserved.

1. Introduction

Multiscale phenomena or processes widely exist in material science, chemical engineering, mechanical engineering, and energy and environmental engineering. It is not exaggerate to say that almost all problems have multiple scales in nature [1]. From the engineering computation point of view, multiscale problems in the thermo-fluid science and engineering as well as in energy and environmental engineering may be classified into two categories: multiscale system and multiscale process [2,3]. A multiscale system refers to a system that is characterized by large variation in length scales in which the processes at different length scale often have the same governing equations and are not closely related [2,3]. Cooling in data centers is a typical multiscale system. The cooling process from the room to the chip involves an extended span of length of about 11 orders while all the fluid flow and heat transfer phenomena in the different length scale can be formulated by Navier–Stokes (NS) equation and the conventional energy conservation equation. In a multiscale process, the overall behavior is governed by processes that occur at different length and/or time scales which are inherently and closely coupled with each other, and the phenomena at different length scales are governed by different equations [2–4]. Proton exchange membrane fuel cell (PEMFC) and turbulent flow and heat transfer are two typical examples

of multiscale process. In a PEMFC, processes of fluid flow, heat and mass transfer, and electronic and proton conduction in different components of a PEMFC with different length scales (gas channel (GC) in the scale of cm, gas diffusion layer (GDL) in the scale of hundred of micrometers, catalyst layer (CL) in the nanometers, and membrane in the scale of hundred of micrometers) are closely related and the processes at different scales are formulated by different equations. The overall cell performance is the combined results of these strongly interacted processes.

Simulation and modeling of the multiscale systems or processes has been rapidly expanded in recent years. In the aspect of modeling multiscale system, a top-to-down sequential multilevel simulation method with increasing fineness of grids has been proposed to simulate velocity and temperature distribution in a data center in Refs. [5,6]. Simulation of a multiscale process is more challenging and attractive due to the more complicated and coupled processes involved in the multiscale process [2,3,7]. In this study, emphasis is placed on the simulation of multiscale processes.

Two types of numerical approaches exist in the literature for the simulation and modeling of multiscale processes in thermo-fluid engineering and science [3]. One can be described as "Using uniform governing equation and solving for the entire domain", for which direct numerical simulation (DNS) is a typical example [8]. In the direct numerical simulation of turbulent heat transfer, in order to resolve the smallest eddies both the space and time steps have to be very fine, making its applications to complicated engineering problems exhibited. The second approach is described as "Solving problems regionally and coupling at the interfaces"

Nomenclature

c	lattice speed	α	transfer coefficient
c_s	lattice sound speed	β	coefficient of solutal expansion
C	compression operator	ϕ	variable
D	diffusivity	η	surface over-potential
D2Q9	2-dimension 9-velocity lattice	v	kinematic viscosity
f	density distribution function (DF)	ρ	density
g	concentration DF; gravity acceleration	τ	relaxation time
H	height	ω	weight factor
l_0	length scale	Γ	nominal diffusion coefficient
L	length		
J	specially chosen constant in Eq. (8)cathode transfer current density	*Superscript*	
		eq	equilibrium
k	reaction rate in Eq. (52)		
K	specially chosen constant in Eq. (8)	*Subscripts*	
n	normal	c	cold side
Nu	Nusselt number	h	hot side
p	pressure	i	direction of the discretized velocity
Pe	Peclet number	in	inlet
R	gas constant	L	lattice unit
Ra	solutal or thermal Rayleigh number	m	average
S	source term	max	maximum
Sc	Schmidt number	min	minimum
T	temperature	o	oxygen
t	time	n	nitrogen
t_0	time scale	p	physical unit
u, v	velocities along in x, y directions	w	water vapor
x, y	cartesian coordinates	ref	reference
Y	concentration	α, β, γ	coordinate direction indexes
Δx	space step		
Δt	time step		

(hereafter called coupled modeling strategy). In this approach, instead of pursuing a single uniform numerical method for the entire domain, a coupled modeling strategy is proposed, in which different numerical methods are used to predict transport process in different local regimes and information is exchanged at the interfaces between neighboring regimes obeying certain principles.

The coupled modeling strategy promotes a better utilization of different numerical methods. Generally, numerical simulation methods in thermo-fluid engineering and science can be divided into three levels, namely numerical methods at macroscopic level (including the finite-difference method (FDM), the finite-element method (FEM), and the finite-volume method (FVM)), at mesoscopic level (including the lattice Boltzmann method (LBM) and the direct-simulation Monte Carlo method (DSMC)) and at microscopic level (including molecular dynamic simulation (MDS) and quantum molecular simulation (QMS)). Macroscopic numerical methods possess the advantages of high computational efficiency, while suffer the disadvantages of lack of important details in some special regimes and the necessity of introducing empirical closures. Mesoscopic or microscopic methods can predict the fundamental details of transport processes but require large and even prohibitive computational resources. The coupled modeling strategy can avoid the disadvantages of the numerical methods at different levels and take the advantages of these numerical methods to some extent. In the implementation of coupled modeling strategy, the computational domain is divided into subdomains and in each subdomain the appropriate numerical method is applied. For example, in PEMFC, reactants transport from the macro GC, through the porous GDL and finally reach the micro CL. When simulating such transport processes by using coupled modeling strategy, a PEMFC can be divided into three subdomains, namely,

GC, GDL and CL. Then, FVM is applied to model the GC, LBM for GDL, LBM or MD for CL. Therefore, advantages of different numerical methods are fully used, leading to both important details of the transport process in complex porous GDL and CL available and computational cost acceptable. Currently, this coupled modeling strategy is experiencing a rapid growth in the modeling of multi-scale processes [7,9–14].

The critical task and chief difficulty in the coupled modeling strategy is how to exchange information at the interface of neighboring subdomains, or essentially between different numerical methods [3,7,15]. For the coupling between LBM and FVM, it is straightforward to transfer the distribution functions obtained in the LBM framework to macro variables (velocity, density, temperature, concentration and so on) through statistic methods [16]. However, evaluation of the distribution function in LBM from macroscopic variables is not straightforward, since the expansion of small amount of macroscopic variables into a large amount of particle distribution functions in LBM is not unique and quite difficult to be implemented [3,15]. Recently the author's group has made some efforts to transfer macro velocity and temperature to particle distribution functions in LBM [7,15,17,18]. In this study, we go on further in this direction to construct principles for transferring species concentration to concentration distribution functions in LBM.

The rest of the present study is organized as follows. First, the fluid flow LB model and diffusion LB model is presented in Section 2. Then, the reconstruction operator for density–velocity distribution function and reconstruction operator for concentration distribution function are derived in Section 3. The coupling scheme between FVM and LBM is also introduced in Section 3. The proposed reconstruction operator and coupling scheme are then

validated by several Diffusion-convection related problems in Section 4. Then, the coupling scheme is applied to simulate the fluid flow and reactant transport process in the cathode side of a PEMFC in Section 5. Finally, some conclusions are given in Section 6.

2. Brief introduction to LBM and FVM

2.1. LBM

Due to its excellent numerical stability and constitutive versatility, LBM has developed into an alternative and promising numerical approach for wide applications in recent years [19–22] and is particularly successful in applications involving interfacial dynamics and complex geometries [16]. LBM simulates pseudo-fluid particles on a mesoscopic level based on Boltzmann equation using a small number of velocities adapted to a regular grid in space. The obvious advantages of LBM are the simplicity of programming, the parallelism of the algorithm and the capability of incorporating complex microscopic interactions. For simplicity, only a brief introduction for fluid flow and species transport LB models is given in the following paragraphs.

2.1.1. LB model for fluid flow

The LB fluid flow model employed is based on the simple and popular Bhatnagar-Gross–Krook (BGK) method [23]. **DnQb** lattice is adopted where n denotes the dimension and b represents number of discrete velocities [24,25]. The evolution of LB equation is described by

$$f_i(x + c_i\Delta t, t + \Delta t) - f_i(x,t) = -\frac{1}{\tau_\upsilon}(f_i(x,t) - f_i^{eq}(x,t)) \tag{1}$$

where $f_i(x,t)$ is the particle distribution function with velocity c_i at the lattice site x and time t, $f_i^{(eq)}$ is the ith equilibrium distribution function, Δt is the time increment, and τ is the collision time. c_i is the discrete velocities. For **D2Q9** model in this study, c_i is given by

$$c_i = \begin{cases} 0 & i = 0 \\ \left(\cos\left[\frac{(i-1)\pi}{2}\right], \sin\left[\frac{(i-1)\pi}{2}\right]\right) & i = 1, 2, 3, 4 \\ \sqrt{2}\left(\cos\left[\frac{(i-5)\pi}{2} + \frac{\pi}{4}\right], \sin\left[\frac{(i-5)\pi}{2} + \frac{\pi}{4}\right]\right) & i = 5, 6, 7, 8 \end{cases} \tag{2}$$

The equilibrium distribution function is given by

$$f_i^{(eq)} = \omega_i \rho \left[1 + \frac{3}{c^2}(c_i \cdot u) + \frac{9}{2c^4}(c_i \cdot u)^2 - \frac{3}{2c^2}u^2\right] \tag{3}$$

where the weights $w_i = 4/9$, $i = 0$; $w_i = 1/9$, $i = 1, 2, 3, 4$; $w_i = 1/36$, $i = 5, 6, 7, 8$. c_s is the sound speed ($c_s = c/\sqrt{3}$ where c equals $\Delta x/\Delta t$). Fluid density ρ and velocity u can be obtained from the first and second moments of the particle distribution functions

$$\rho = \sum_i f_i, \tag{4}$$

$$\rho u = \sum_i f_i c_i \tag{5}$$

The kinematics viscosity in lattice unit is related to the collision time by

$$v = c_s^2(\tau_v - 0.5)\Delta t \tag{6}$$

2.1.2. LB model for species transport

For species transport with reactions, the evolution of LB equation is described by Dawson et al. [26]

$$g_i(x + c_i\Delta t, t + \Delta t) - g_i(x,t) = -\frac{1}{\tau_Y}(g_i(x,t) - g_i^{eq}(x,t)) \tag{7}$$

where g_i is the concentration distribution function. The equilibrium concentration distribution function $g_i^{eq}(x,t)$ is commonly chosen as [27]

$$g_i^{eq} = Y_k[J_i + K_i c_i \cdot u] \tag{8}$$

where K_i is constant and equals 1/2 for two-dimensional case. Y is the concentration.

For mass transport simulation, the **D2Q9** square lattice for 2D simulation can be reduced to **D2Q5** square lattice by ignoring velocities at the diagonals, namely four velocities with subscript i greater than 4 in Eq. (2). This reduction of discrete velocities doesn't create loss of accuracy [27].

J_i in Eq. (8) is given by [27]

$$J_i = \begin{cases} J_0, & i = 0 \\ (1 - J_0)/4, & i = 1, 2, 3, 4 \end{cases} \tag{9}$$

where the rest fraction J_0 can be selected from 0 to 1 depending on the diffusivity D. Species concentration Y is obtained by

$$Y = \sum g_i \tag{10}$$

The diffusivity in lattice unit is related to the collision time by

$$D = C_Q(1 - J_0)(\tau_D - 0.5)\frac{\Delta x^2}{\Delta t} \tag{11}$$

where C_Q is a lattice dependent coefficient and equals 1/2 for 2D simulation [27].

2.2. FVM

FVM is the most widely adopted numerical method at macroscopic level for numerical fluid flow and heat transfer due to its conservation properties of the discretized equation and the clear physical meaning of the coefficients. The differential governing equations are as follows

$$\frac{\partial(\rho\phi)}{\partial t} + \nabla(\rho u\phi) = \nabla(\Gamma_\phi \nabla\phi) + S_\phi \tag{12}$$

where ϕ is a scalar dependent variable (such as velocity component, temperature and concentration). Γ is the nominal diffusion coefficient, and S_ϕ is the source term.

SIMPLE algorithm proposed by Patankar and Spalding in 1972 is the most well-known solution procedure based on FVM for solving NS equations, which are included in Eq. (12). There are two major assumptions in the SIMPLE algorithm: (1) the initial pressure and initial velocity are independently assumed, leading to some inconsistency between p and u, v; and (2) when the velocity correction equation is derived, the effects of the neighboring grids' velocity corrections are totally neglected. These two assumptions do not affect the final solution but do affect the convergence rate. The first assumption was overcome by SIMPLER of Patankar [28]. Many efforts have been devoted to overcome the second assumption and several solution procedures have been proposed such as SIMPLEC [29], PISO [30], the explicit correction-step method [31], and MSIMPLER [32]. However, none of the above solution procedures could completely overcome the second assumption. In recent years, two solution algorithms called CLEAR [33,34] and IDEAL [35,36] are developed by the author's group, in which the second assumption is completely deleted, making the algorithm fully implicit. In the CLEAR algorithm, the improved pressure and velocity are solved directly, rather than by adding a correction term to the intermediate solution. The IDEAL algorithm further improves the convergence rate and robustness of the CLEAR by updating the pressure equations repeatedly in both prediction and correction steps.

In this article, the two-dimensional (2D) IDEAL collocated grid algorithm is adopted [35,36], and the SGSD scheme [37] is used to discretize the convective term.

3. The coupling principle between FVM and LBM

3.1. Reconstruction operator for density–velocity distribution function

Attention now is turned to design coupled principle between FVM and LBM. As mentioned above, the critical task and chief difficulty in the coupling between FVM and LBM is to transfer macroscopic variables to distribution functions in LBM. As indicated above, our groups have made some efforts to transfer macro velocity and temperature to particle distribution functions in LBM [7,15,17,18]. For the readers' convenience and also for further derivation of species transport coupling scheme, the derivation process of the density distribution function is briefly presented below [15].

According to the Chapman–Enskog method, we can introduce the following time and space scale expanding

$$\partial_t = \varepsilon \partial_t^{(1)} + \varepsilon^2 \partial_t^{(2)} \tag{13a}$$

$$\partial_{x_\alpha} = \varepsilon \partial_{x_\alpha}^{(1)} \tag{13b}$$

the small expansion parameter ε can be viewed as the Knudsen number Kn which is the ratio of the mean free path over the characteristic length scale of the flow, and α represents the two coordinate directions.

The distribution function f_i is expanded around the distributions $f_i^{(0)}$ as follows

$$f_i = f_i^{(0)} + \varepsilon f_i^{(1)} + \varepsilon^2 f_i^{(2)} \tag{14}$$

with

$$\sum_i f_i^{(1)} = 0, \quad \sum_i c_i f_i^{(1)} = 0, \quad \sum_i f_i^{(2)} = 0, \quad \sum_i c_i f_i^{(2)} = 0 \tag{15}$$

Then, $f_i(\boldsymbol{x} + \boldsymbol{c}_i \Delta t, t + \Delta t)$ in Eq. (1) is expanded about x and t which gives

$$f_i(\boldsymbol{x} + \boldsymbol{c}_i \Delta t, t + \Delta t) = f_i(\boldsymbol{x}, t) + \Delta t D_{i\alpha} f_i(\boldsymbol{x}, t) + \frac{(\Delta t)^2}{2} D_{i\alpha}^2 f_i(\boldsymbol{x}, t)$$
$$+ O\left[(\Delta t)^3\right] \tag{16}$$

where $D_{i\alpha} = \partial_t + c_i \partial_{x_\alpha}$ for concise expression.

Substituting Eq. (16) into Eq. (1) yields the following equation

$$\Delta t D_{i\alpha} f_i + \frac{(\Delta t)^2}{2} D_{i\alpha}^2 f_i = -\frac{1}{\tau_f}\left(f_i - f_i^{(eq)}\right) + O\left[(\Delta t)^3\right] \tag{17}$$

Furthermore, substituting Eqs. (13a), (13b) and (14) into Eq. (17) obtains

$$\varepsilon D_{i\alpha}^{(1)} f^{(0)} + \varepsilon^2 \left[D_{i\alpha}^{(1)} f_i^{(1)} + \partial_t^{(2)} f_i^{(0)}\right] + \varepsilon^2 \frac{\Delta t}{2}\left[D_{i\alpha}^{(1)}\right]^2 f_i^{(0)}$$
$$= -\frac{1}{\Delta t \tau_f}\left(f_i^{(0)} + \varepsilon f_i^{(1)} + \varepsilon^2 f_i^{(2)} - f_i^{(eq)}\right) + O\left[(\Delta t)^3\right] \tag{18}$$

Then by matching the scales of ε^0, ε^1 and ε^2, we have

$$\varepsilon^0 : f_i^{(0)} = f_i^{(eq)} \tag{19}$$

$$\varepsilon^1 : f_i^{(1)} = -\Delta t \tau_f D_{i\alpha}^{(1)} f^{(0)} + O\left[(\Delta t)^2\right] \tag{20}$$

$$\varepsilon^2 : f_i^{(2)} = -\Delta t \tau_f \left[D_{i\alpha}^{(1)} f_i^{(1)} + \partial_t^{(2)} f_i^{(0)}\right] - \tau_f \frac{(\Delta t)^2}{2}\left[D_{i\alpha}^{(1)}\right]^2 f_i^{(0)} + O\left[(\Delta t)^3\right] \tag{21}$$

Considering Eqs. (4) and (5), we can sum Eq. (20) over the phase space. Then the first order of the continuity equation and momentum equation can be derived.

$$\varepsilon^1 : \partial_t^{(1)} \rho + \partial_{x_\alpha}^{(1)} (\rho u_\alpha) + O[(\Delta t)^2] = 0 \tag{22a}$$

$$\partial_t^{(1)} (\rho u_\alpha) + \partial_{x_\beta}^{(1)} (\rho u_\alpha u_\beta + p \delta_{\alpha\beta}) + O[(\Delta t)^2] = 0 \tag{22b}$$

By the same way, we can obtain the second order of continuity equation and momentum equation according to Eq. (21)

$$\varepsilon^2 : \partial_t^{(2)} \rho + O\left[(\Delta t)^3\right] = 0 \tag{23a}$$

$$\partial_t^{(2)} (\rho u_\alpha) - v \partial_{x_\beta}^{(1)} \left\{\rho \left[\partial_{x_\alpha}^{(1)} u_\beta + \partial_{x_\beta}^{(1)} u_\alpha\right]\right\} + O\left[(\Delta t)^3\right] = 0 \tag{23b}$$

The formulas according to the chain rule of derivatives read:

$$\partial_t f_i^{(eq)} = \partial_\rho f_i^{(eq)} \partial_t \rho + \partial_{u_\beta} f_i^{(eq)} \partial_t u_\beta \tag{24a}$$

$$\partial_{x_\alpha} f_i^{(eq)} = \partial_\rho f_i^{(eq)} \partial_{x_\alpha} \rho + \partial_{u_\beta} f_i^{(eq)} \partial_{x_\alpha} u_\beta \tag{24b}$$

From Eq. (3), we can get

$$\partial_{u_\beta} f_i^{(eq)} = \omega_i \rho \left[\frac{1}{c_s^2}(c_{i\beta} - u_\beta) + \frac{1}{c_s^4} c_{i\alpha} c_{i\beta} u_\alpha\right] \tag{25}$$

$$\partial_\rho f_i^{(eq)} = \frac{1}{\rho} f_i^{(eq)} \tag{26}$$

Furthermore, substituting (25) and (26) into Eq. (20), we can derive the first order expression of distribution function f_i

$$f_i^{(1)} = -\tau_f \Delta t \left[\partial_t^{(1)} f_i^{(0)} + c_i \partial_{x_\alpha}^{(1)} f_i^{(0)}\right]$$
$$= -\tau_f \Delta t \left[\partial_\rho f_i^{(0)} \partial_t^{(1)} \rho + \partial_{u_\beta} f_i^{(0)} \partial_t^{(1)} u_\beta + c_i \left(\partial_\rho f_i^{(0)} \partial_{x_\alpha}^{(1)} \rho + \partial_{u_\beta} f_i^{(0)} \partial_{x_\alpha}^{(1)} u_\beta\right)\right]$$
$$= -\tau_f \Delta t \left[U_{i\alpha} f_i^{(0)} \frac{1}{\rho} \partial_{x_\alpha}^{(1)} \rho + U_{i\alpha} \omega_i \rho \left(\frac{1}{c_s^2} U_{i\beta} + \frac{1}{c_s^4} c_{i\beta} c_{i\gamma} u_\gamma\right) \partial_{x_\alpha}^{(1)} u_\beta - f_i^{(0)} \partial_{x_\alpha}^{(1)} u_\alpha\right.$$
$$\left. - \omega_i \left(\frac{1}{c_s^2} U_{i\alpha} + \frac{1}{c_s^4} c_{i\alpha} c_{i\gamma} u_\gamma\right) \partial_{x_\alpha}^{(1)} p\right] \tag{27}$$

where $U_{i\alpha} = c_{i\alpha} - u_\alpha$.

The second-order expression of f_i in Eq. (21) is calculated as follows

$$f_i^{(2)} = -\Delta t \tau_f \left[D_{i\alpha}^{(1)} f_i^{(1)} + \partial_t^{(2)} f_i^{(0)}\right] - \frac{(\Delta t)^2 \tau_f}{2}\left[D_{i\alpha}^{(1)}\right]^2 f_i^{(0)}$$
$$= -\Delta t \tau_f \left[D_{i\alpha}^{(1)} \left(-\tau \Delta t D_{i\alpha}^{(1)} f_i^{(0)}\right) + \partial_t^{(2)} f_i^{(0)}\right]$$
$$- \frac{(\Delta t)^2 \tau_f}{2}\left[D_{i\alpha}^{(1)}\right]^2 f_i^{(0)}$$
$$= -\Delta t \tau_f \partial_t^{(2)} f_i^{(0)} + (\Delta t)^2 \tau_f \left(\tau_f - \frac{1}{2}\right)\left[D_{i\alpha}^{(1)}\right]^2 f_i^{(0)} \tag{28}$$

We can ignore the second-order derivative of $f_i^{(2)}$, then

$$f_i^{(2)} = -\Delta t \tau_f \partial_t^{(2)} f_i^{(0)} \tag{29}$$

By the chain rule of derivatives, it gives

$$\partial_t^{(2)} f_i^{(0)} = \partial_\rho f_i^{(0)} \partial_t^{(2)} \rho + \partial_{u_\beta} f_i^{(0)} \partial_t^{(2)} u_\beta = \partial_{u_\beta} f_i^{(0)} \partial_t^{(2)} u_\beta \tag{30}$$

Using Eqs. (23b) and (25), we get

$$\partial_t^{(2)} f_i^{(0)} = \partial_{u_\beta} f_i^{(0)} \partial_t^{(2)} u_\beta = \frac{1}{\rho} \partial_{u_\beta} f_i^{(0)} \partial_t^{(2)} (\rho u_\beta)$$
$$= v \omega_i \left[\frac{1}{c_s^2}(c_{i\beta} - u_\beta) + \frac{1}{c_s^4} c_{i\alpha} c_{i\beta} u_\alpha\right] \partial_{x_\alpha}^{(1)} \left(\rho \left(\partial_{x_\alpha}^{(1)} u_\beta + \partial_{x_\beta}^{(1)} u_\alpha\right)\right)$$
$$= v \omega_i \rho \left[\frac{1}{c_s^2}(c_{i\beta} - u_\beta) + \frac{1}{c_s^4} c_{i\alpha} c_{i\beta} u_\alpha\right] \left[\frac{1}{\rho} \partial_{x_\alpha}^{(1)} \rho \left(\partial_{x_\alpha}^{(1)} u_\beta + \partial_{x_\beta}^{(1)} u_\alpha\right)\right.$$
$$\left. + \partial_{x_\alpha}^{(1)} \left(\partial_{x_\alpha}^{(1)} u_\beta + \partial_{x_\beta}^{(1)} u_\alpha\right)\right] \tag{31}$$

So the following expression is obtained

$$f_i^{(2)} = -\Delta t \tau_f v \omega_i \rho \left(\frac{1}{c_s^2} U_{i\beta} + \frac{1}{c_s^4} c_{i\alpha} c_{i\beta} u_\alpha\right) \left[\frac{1}{\rho} \partial_{x_\alpha}^{(1)} \rho \left(\partial_{x_\alpha}^{(1)} u_\beta + \partial_{x_\beta}^{(1)} u_\alpha\right)\right.$$
$$\left. + \partial_{x_\alpha}^{(1)} \left(\left(\partial_{x_\alpha}^{(1)} u_\beta + \partial_{x_\beta}^{(1)} u_\alpha\right)\right)\right] \tag{32}$$

Here, we introduce an approximation of $\partial_{u_\beta} f_i^{(0)}$ by dropping terms of a higher order than u^2 as follows

$$\partial_{u_\beta} f_i^{(0)} = \omega_i \rho \left(\frac{1}{c_s^2} U_{i\beta} + \frac{1}{c_s^4} c_{i\beta} c_{i\gamma} u_\gamma \right) \approx \frac{U_{i\beta}}{c_s^2} f_i^{(0)} \tag{33}$$

Assuming the velocity fields is divergence-free, written as

$$\partial_{x_\alpha} u_\alpha = 0. \tag{34}$$

According to Eqs. (33) and (34), we can rewrite the expressions of $f_i^{(1)}$ and $f_i^{(2)}$ as

$$
\begin{aligned}
f_i^{(1)} &= -\tau_f \Delta t \left[U_{i\alpha} f_i^{(0)} \frac{1}{\rho} \partial_{x_\alpha}^{(1)} \rho + U_{i\alpha} U_{i\beta} f_i^{(0)} \frac{1}{c_s^2} \partial_{x_\alpha}^{(1)} u_\beta - U_{i\alpha} f_i^{(0)} \frac{1}{\rho c_s^2} \partial_{x_\alpha}^{(1)} p \right] \\
&= -\tau_f \Delta t U_{i\alpha} U_{i\beta} f_i^{(0)} c_s^{-2} \partial_{x_\alpha}^{(1)} u_\beta
\end{aligned}
\tag{35}
$$

$$
\begin{aligned}
f_i^{(2)} &= -\Delta t \tau_f \nu U_{i\beta} f_i^{(0)} c_s^{-2} \left[\frac{1}{\rho} \partial_{x_\alpha}^{(1)} \rho \left(\partial_{x_\alpha}^{(1)} u_\beta + \partial_{x_\beta}^{(1)} u_\alpha \right) + \left(\partial_{x_\alpha}^{(1)} \right)^2 u_\beta \right] \\
&= -\Delta t \tau_f \nu U_{i\beta} f_i^{(0)} c_s^{-2} \left[\frac{1}{\rho} S_{\alpha\beta}^{(1)} \partial_{x_\alpha}^{(1)} \rho + \left(\partial_{x_\alpha}^{(1)} \right)^2 u_\beta \right]
\end{aligned}
\tag{36}
$$

where $S_{\alpha\beta} = \partial_{x_\beta} u_\alpha + \partial_{x_\alpha} u_\beta$.

Finally, we can derive the expression of f_i

$$
\begin{aligned}
f_i &= f_i^{(0)} + \varepsilon f_i^{(1)} + \varepsilon^2 f_i^{(2)} \\
&= f_i^{(0)} - \tau \Delta t U_{i\alpha} U_{i\beta} f_i^{(0)} c_s^{-2} \partial_{x_\alpha} u_\beta \\
&\quad - \tau \Delta t \nu U_{i\beta} f_i^{(0)} c_s^{-2} \left[\frac{1}{\rho} S_{\alpha\beta} \partial_{x_\alpha} \rho + \partial_{x_\alpha}^2 u_\beta \right] \\
&= f_i^{(eq)} \left[1 - \tau \Delta t U_{i\beta} c_s^{-2} \left(U_{i\alpha} \partial_{x_\alpha} u_\beta + \nu \partial_{x_\alpha}^2 u_\beta + \nu \rho^{-1} S_{\alpha\beta} \partial_{x_\alpha} \rho \right) \right]
\end{aligned}
\tag{37}
$$

Eq. (37) is an analytic expression for reconstructing the density–velocity distribution function from the macro variables. Hereafter we call it as density–velocity distribution function reconstruction operator.

3.2. Reconstruction operator for concentration distribution function

Now attention is turned to develop the reconstruction operator for concentration distribution function which is the major concern of the present study. Following Eqs. (14)–(21), we can obtain g_i in the scales of ε^0, ε^1 and ε^2

$$\varepsilon^0 : g_i^{(0)} = g_i^{(eq)} \tag{38}$$

$$\varepsilon^1 : g_i^{(1)} = -\Delta t \tau_g D_{i\alpha}^{(1)} g_i^{(0)} + O\left[(\Delta t)^2 \right] \tag{39}$$

$$\varepsilon^2 : g_i^{(2)} = -\Delta t \tau_g \left[D_{i\alpha}^{(1)} g_i^{(1)} + \partial_t^{(2)} g_i^{(0)} \right] - \frac{(\Delta t)^2 \tau_g}{2} \left[D_{i\alpha}^{(1)} \right]^2 g_i^{(0)} + O\left[(\Delta t)^3 \right] \tag{40}$$

Therefore, we can derive the macroscopic equations at the $t_1 = \varepsilon t$ and $t_2 = \varepsilon^2 t$ time scales

$$\partial_t^{(1)} Y + \partial_{x_\alpha}^{(1)} (u_\alpha Y) = 0 \tag{41}$$

$$\partial_t^{(2)} Y - 2J(\tau - 0.5) \frac{\Delta x^2}{\Delta t} \partial_{x_\alpha}^{(1)} \partial_{x_\alpha}^{(1)} (Y) = 0 \tag{42}$$

Introducing the formulas according to the chain rule of derivatives

$$\partial_t g_i^{(eq)} = \partial_Y g_i^{(eq)} \partial_t Y + \partial_{u_\beta} g_i^{(eq)} \partial_t u_\beta \tag{43}$$

$$\partial_{x_\alpha} g_i^{(eq)} = \partial_Y g_i^{(eq)} \partial_{x_\alpha} Y + \partial_{u_\beta} g_i^{(eq)} \partial_{x_\alpha} u_\beta \tag{44}$$

and from the equilibrium distribution function given by Eq. (8), we can get the following expression

$$\partial_{u_\beta} g_i^{(eq)} = \partial_{u_\beta} [Y(J + 1/2 c_{i\gamma} u_\gamma)] = 1/2 Y c_{i\beta} \tag{45}$$

$$\partial_Y g_i^{(eq)} = \partial_Y [Y(1 + 1/2 c_{i\gamma} u_\gamma)] = Y^{-1} g_i^{(eq)} \tag{46}$$

The first order expression of distribution function g_i can be derived as

$$
\begin{aligned}
g_i^{(1)} &= -\tau_g \Delta t D_i^{(1)} g_i^{(0)} = -\tau_g \Delta t \left(\partial_t^{(1)} g_i^{(0)} + c_{i\alpha} \partial_{x_\alpha}^{(1)} g_i^{(0)} \right) \\
&= -\tau_g \Delta t \left[\partial_Y g_i^{(0)} \partial_t^{(1)} Y + \partial_{u_\beta} g_i^{(0)} \partial_t^{(1)} u_\beta + c_{i\alpha} \left(\partial_Y g_i^{(0)} \partial_{x_\alpha}^{(1)} Y + \partial_{u_\beta} g_i^{(0)} \partial_{x_\alpha}^{(1)} u_\beta \right) \right] \\
&= -\tau_g \Delta t \left[-\partial_Y g_i^{(0)} \partial_{x_\alpha}^{(1)} (u_\alpha Y) - u_\alpha \partial_{u_\beta} g_i^{(0)} \partial_{x_\alpha}^{(1)} u_\beta - \frac{1}{\rho} \partial_{u_\beta} g_i^{(0)} \partial_{x_\beta}^{(1)} p \right. \\
&\quad \left. + c_{i\alpha} \left(\partial_Y g_i^{(0)} \partial_{x_\alpha}^{(1)} Y + \partial_{u_\beta} g_i^{(0)} \partial_{x_\alpha}^{(1)} u_\beta \right) \right] \\
&= -\tau_g \Delta t \left[U_{i\alpha} Y^{-1} g_i^{(eq)} \partial_{x_\alpha}^{(1)} Y + 0.5 U_{i\alpha} Y c_{i\beta} \partial_{x_\alpha}^{(1)} u_\beta - 0.5 \rho^{-1} Y c_{i\beta} \partial_{x_\beta}^{(1)} p \right] \tag{47}
\end{aligned}
$$

The second order expression of distribution function g_i can be derived as

$$
\begin{aligned}
g_i^{(2)} &= -\tau_g \Delta t \left\{ \partial_t^{(2)} g_i^{(0)} + \left(1 - \frac{1}{2\tau_g} \right) D_i^{(1)} g_i^{(1)} \right\} \\
&= -\tau_g \Delta t \left\{ \partial_t^{(2)} g_i^{(0)} - \left(\tau_g - \frac{1}{2} \right) \Delta t D_i^{(1)} \left[D_i^{(1)} g_i^{(0)} \right] \right\} \\
&= -\tau_g \Delta t \left[\partial_t^{(2)} g_i^{(0)} - \left(\tau_g - \frac{1}{2} \right) \Delta t \left(D_i^{(1)} \right)^2 g_i^{(0)} \right] \tag{48}
\end{aligned}
$$

The second-order derivative of $g_i^{(0)}$ can be ignored in the above equation, then

$$
\begin{aligned}
g_i^{(2)} &= -\tau_g \Delta t \partial_t^{(2)} g_i^{(0)} = -\tau_g \Delta t \left[\partial_Y g_i^{(0)} \partial_t^{(2)} Y + \partial_{u_\beta} g_i^{(0)} \partial_t^{(2)} u_\beta \right] \\
&= -\tau_g \Delta t \left[DY^{-1} g_i^{(eq)} \partial_{x_\alpha}^{(1)} \partial_{x_\alpha}^{(1)} Y + 0.5 Y c_{i\beta} \rho^{-1} \partial_{t_2} (\rho u_\beta) \right] \\
&= -\tau_g \Delta t \left[DY^{-1} g_i^{(eq)} \partial_{x_\alpha}^{(1)} \partial_{x_\alpha}^{(1)} Y + 0.5 Y c_{i\beta} \rho^{-1} \nu \left[\rho \partial_{x_\alpha}^{(1)} \left(\left(\partial_{x_\alpha}^{(1)} u_\beta + \partial_{x_\beta}^{(1)} u_\alpha \right) \right) \right. \right. \\
&\quad \left. \left. + \left(\partial_{x_\alpha}^{(1)} u_\beta + \partial_{x_\beta}^{(1)} u_\alpha \right) \partial_{x_\alpha}^{(1)} \rho \right] \right] \\
&= -\tau_g \Delta t \left[DY^{-1} g_i^{(eq)} \partial_{x_\alpha}^{(1)} \partial_{x_\alpha}^{(1)} Y + 0.5 Y c_{i\beta} \rho^{-1} \nu \left[\rho \partial_{x_\alpha}^{(1)} \partial_{x_\alpha}^{(1)} u_\beta + S_{\alpha\beta}^{(1)} \partial_{x_\alpha}^{(1)} \rho \right] \right] \tag{49}
\end{aligned}
$$

At last, the expression of g_i is derived as

$$
\begin{aligned}
g_i &= g_i^{(0)} + \varepsilon g_i^{(1)} + \varepsilon^2 g_i^{(2)} + \cdots \\
&= g_i^{(eq)} - \tau_g \Delta t \left[U_{i\alpha} Y^{-1} g_i^{(eq)} \partial_{x_\alpha}^{(1)} Y + 0.5 U_{i\alpha} Y c_{i\beta} \partial_{x_\alpha}^{(1)} u_\beta - 0.5 \rho^{-1} Y c_{i\beta} \partial_{x_\beta}^{(1)} p \right] \\
&\quad - \tau_g \Delta t \left[DY^{-1} g_i^{(eq)} \partial_{x_\alpha} \partial_{x_\alpha} Y + 0.5 Y c_{i\beta} \rho^{-1} \nu [\rho \partial_{x_\alpha} \partial_{x_\alpha} u_\beta + S_{\alpha\beta} \partial_{x_\alpha} \rho] \right] \\
&= g_i^{(eq)} - \tau_g \Delta t \left[U_{i\alpha} Y^{-1} g_i^{(eq)} \partial_{x_\alpha}^{(1)} Y + 0.5 U_{i\alpha} Y c_{i\beta} \partial_{x_\alpha}^{(1)} u_\beta - 0.5 \rho^{-1} Y c_{i\beta} \partial_{x_\beta}^{(1)} p \right] \\
&\quad - \tau_g \Delta t \left[DY^{-1} g_i^{(eq)} \partial_{x_\alpha} \partial_{x_\alpha} Y + 0.5 Y c_{i\beta} \rho^{-1} \nu [\rho \partial_{x_\alpha} \partial_{x_\alpha} u_\beta + S_{\alpha\beta} \partial_{x_\alpha} \rho] \right] \\
&= g_i^{(eq)} \left[1 - \tau_g \Delta t Y^{-1} (U_{i\alpha} \partial_{x_\alpha}^{(1)} Y - D \partial_{x_\alpha} \partial_{x_\alpha} Y) \right] \\
&\quad - 0.5 \tau_g \Delta t Y c_{i\beta} (U_{i\alpha} \partial_{x_\alpha}^{(1)} u_\beta + \nu \partial_{x_\alpha} \partial_{x_\alpha} u_\beta + \rho^{-1} \nu S_{\alpha\beta} \partial_{x_\alpha} \rho) \\
&\quad + 0.5 \tau_g \Delta t \rho^{-1} Y c_{i\beta} c_s^{-2} \partial_{x_\beta}^{(1)} \rho \tag{50}
\end{aligned}
$$

Eq. (50) is an analytic expression for the reconstruction of the concentration distribution function g_i from the macro concentration. It will be called concentration distribution function reconstruction operator.

Eq. (37) combined with Eq. (50) can be applied to the fluid flow and species transport. The reconstruction operations are essential to establish an effective information exchange scheme from macro-solver to the micro-solver and to construct a reasonable initial field for accelerating the microscopic computation.

3.3. Computational procedure

In this section, the basic idea of the computational procedure by coupling FVM and LBM is illustrated. Fig. 1 schematically shows a computational domain decomposed into two regions. FVM and LBM are used to simulate fluid flow and mass transport in the left region and right region respectively. Line MN is the FVM region boundary located in the LBM sub-region, and AB is the LBM region
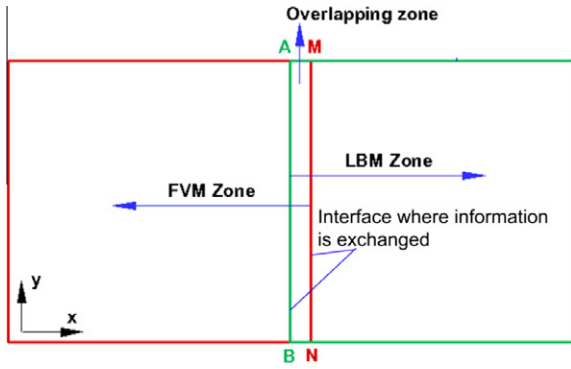
Fig. 1. Computational domain decomposed into two sub-regions.
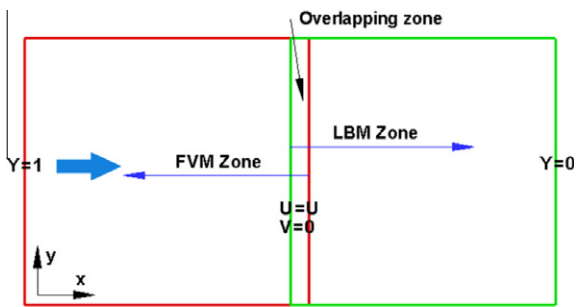

Fig. 2. Schematic computational domain of the diffusion–convection–reaction problem.

boundary located in the FVM sub-region. Hence, the sub-region between lines AB and MN is the overlapping region in which both LBM and FVM methods are adopted. This arrangement of the interface is convenient for the information exchange between the two neighboring regions [2]. In the simulations of this study, the grid size in one sub-region is equal to that in the other sub-region. Obviously, different grid sizes can be adopted in different sub-regions. Under this circumstance, space interpolation at the interface is required to transfer the information at the interface [17], and one can refer to [17] for more information.

Now the computational procedures using coupled FVM and LBM are summarized as follows (hereafter called CFVLBM).

Step 1 . With some assumed initial boundary conditions at the line MN, the FVM simulation in the FVM zone is performed.
Step 2 . After a temporary solution is obtained, the information at the line AB is transformed into the density–velocity distribution function by Eq. (37) and the concentration distribution function by Eq. (50).
Step 3 . The LBM simulation is carried out in the LBM zone.
Step 4 . The temporary solution of LBM at the line MN is transported into the macro variables and the FVM simulation is repeated.
Step 5 . Such computation is repeated until the results at the two lines are remained the same within an allowed tolerance.

4. Validation

In this section, two examples are simulated to validate the CFVLBM coupling modeling strategy. One is diffusion–convection–reaction problem and the other is natural convection in a square called by concentration gradient.
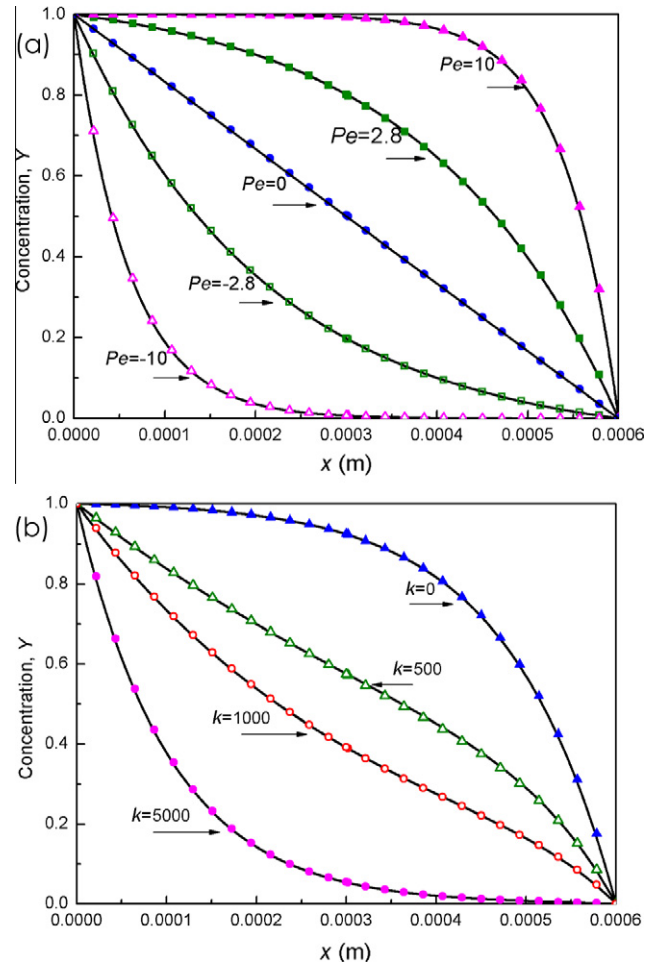

Fig. 3. Comparison between simulation results from the CFVLBM (dot) and analytical solutions (line) for the diffusion–convection–reaction problem. (a) Different Pe number with reaction rate of zero, (b) Different reaction rates with $Pe = 2.8$.
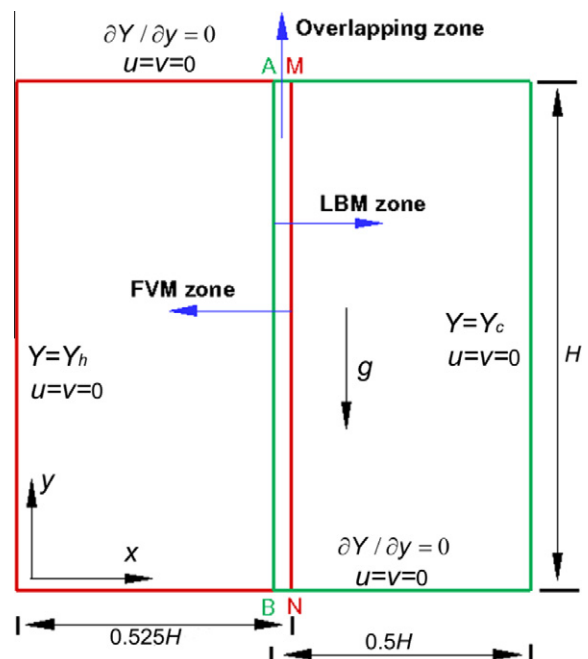

Fig. 4. Computational domain of the natural convection induced by concentration gradient.

(a) CFVLBM simulated results for natural convection caused by concentration gradient

(b) Software FLUENT simulated results for natural convection caused by concentration gradient

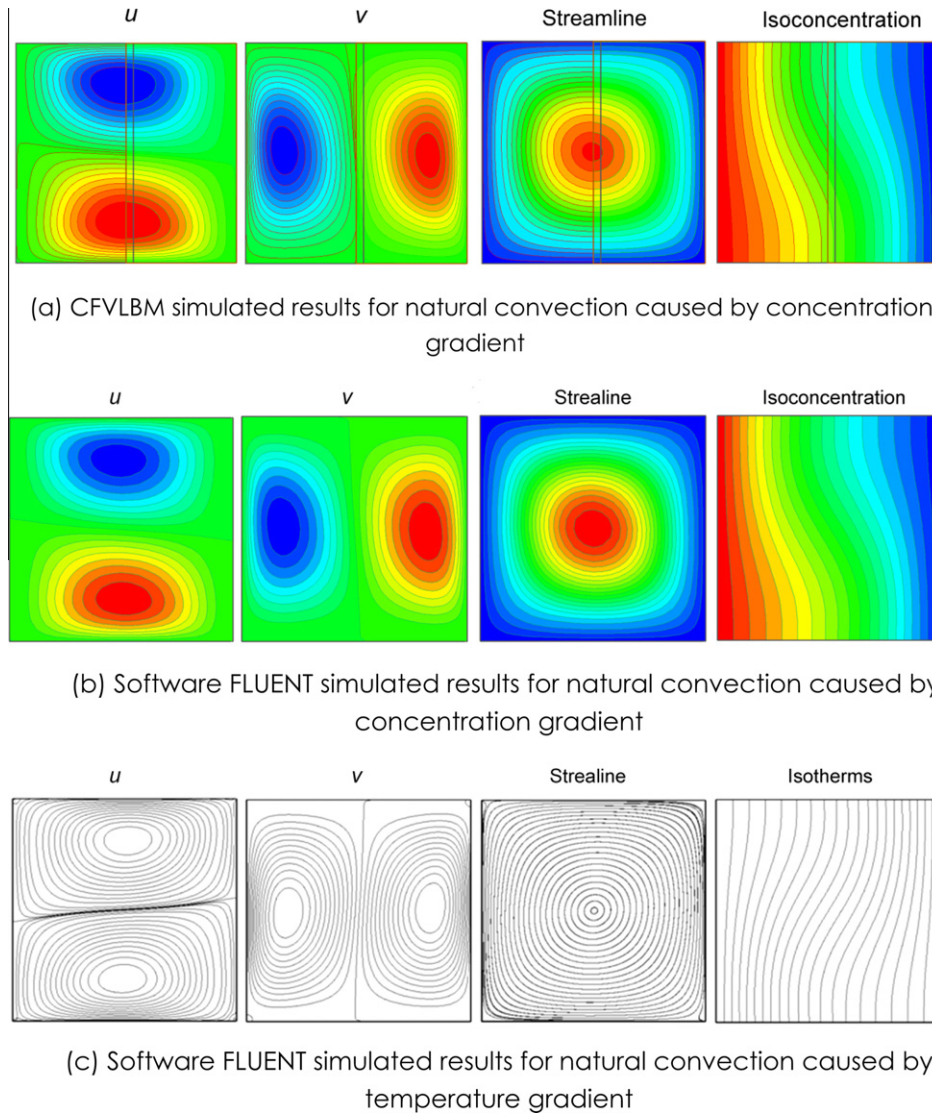(c) Software FLUENT simulated results for natural convection caused by temperature gradient

Fig. 5. Contour lines for natural convection in square cavity for $Sc = 0.71$ ($Pr = 0.71$) and solutal $Ra = 10^3$ (thermal $Ra = 10^3$).

In the LBM model, the simulation variables are in the lattice units instead of physical units. To connect the lattice space to physical space, length scale l_0, time scale t_0 and density scale ρ_0 are chosen in this study. Accordingly, the physical variables such as velocity u_p, pressure p_p, viscosity v_p and diffusivity D_p can be calculated from the quantities in lattice system (subscripted by L) as follows

$$u_P = u_L \frac{l_0}{t_0}, \quad p_P = p_L \rho_0 \left(\frac{l_0}{t_0}\right)^2, \quad D_P = D_L \frac{l_0^2}{t_0}, \quad v_P = v_L \frac{l_0^2}{t_0} \quad (51)$$

In this study, the scale parameters are chosen as $l_0 = 1.0 \times 10^{-6}$ m, $t_0 = 1.33 \times 10^{-8}$ s and $\rho_0 = 1.0$ kg m^{-3}.

4.1. Diffusion–convection–reaction problem

A diffusion–convection–reaction problem is adopted to validate CFVLBM developed in the present work, as shown in Fig. 2. Species transports from the left inlet to the right outlet. At the inlet, species concentration is $Y = 1$, and at the outlet $Y = 0$. A uniform constant horizontal flow with velocity u is injected into the domain from the inlet and is removed from the outlet. Reactions take place in the whole computational domain. Obviously, the above problem

described is essentially one-dimensional. The macroscopic governing equation for species concentration of the above problem is

$$u \frac{dY}{dx} = D \frac{d^2 Y}{dx^2} - kY \quad (52)$$

where k is the reaction rate. The analytical solution of Eq. (52) is

$$Y = A_1 \exp(B_1 x) + A_2 \exp(B_2 x) \quad (53a)$$

where

$$B_1 = \left(\frac{u}{D} - \sqrt{\left(\frac{u}{D}\right)^2 + \frac{4k}{D}}\right) \Big/ 2, \quad B_2 = \left(\frac{u}{D} + \sqrt{\left(\frac{u}{D}\right)^2 + \frac{4k}{D}}\right) \Big/ 2,$$

$$A_1 = \frac{Y_{out} - Y_{in} \exp(B_2 L)}{\exp(B_1) - \exp(B_2 L)}, \quad A_2 = Y_{in} - A_1 \quad (53b)$$

In the simulation, $D = 2.845 \times 10^{-5}$ m^2 s^{-1}. The length and height of the computational domain is $L = 6 \times 10^{-4}$ m and $H = 1 \times 10^{-4}$ m respectively. J_0 in Eq. (10) is 0.2. Uniform grid sizes are adopted for both the FVM and LBM zones with grid size as 1×10^{-6} m. Thus, the grid number of the FVM zone is 311×101 and that of the LBM zone is 301×101. Ten more grids along the x direction for FVM zone are due to the overlapping zone. The boundary conditions for the species transport are non-flux on the bottom and top boundaries.
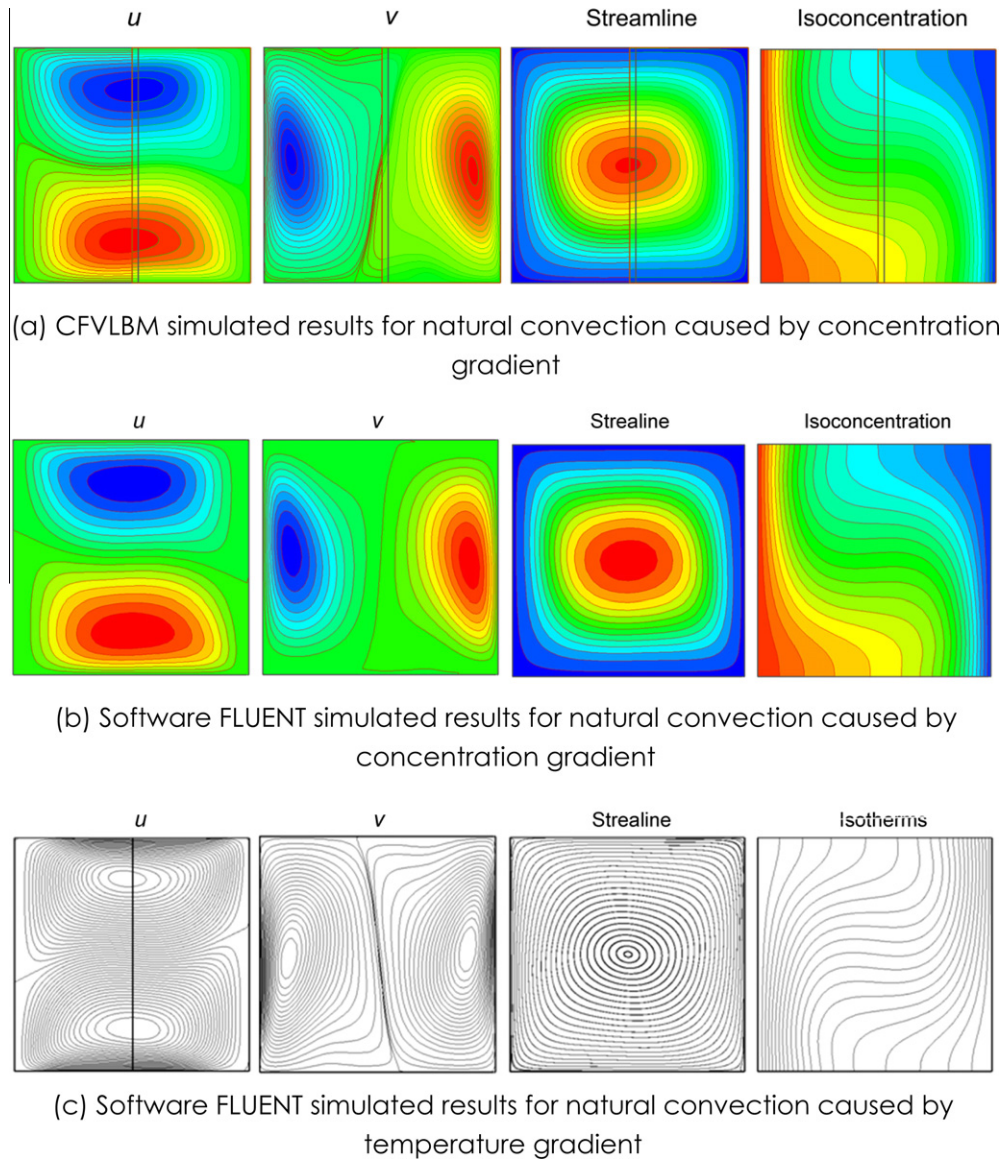
(a) CFVLBM simulated results for natural convection caused by concentration gradient

(b) Software FLUENT simulated results for natural convection caused by concentration gradient

(c) Software FLUENT simulated results for natural convection caused by temperature gradient

Fig. 6. Contour lines for natural convection in square cavity for $Sc = 0.71$ ($Pr = 0.71$) and solutal $Ra = 10^4$ (thermal $Ra = 10^4$).

Fig. 3(a) compares the simulation results of species concentration along x axis with the analytical solutions for different Peclet number Pe, which is defined as u/D. In Fig. 3(a), the reaction rate k is zero, leading to the above problem reduced to a diffusion-convection problem. It can be seen in Fig. 3(a) that the simulation results adopting CFVLBM agree well with the analytical solutions for all the cases, with the maximum deviation less than 0.02 %.

Fig. 3(b) compares the simulation results with the analytical solutions for different reaction rate. In Fig. 3(b) Pe is fixed as 2.8 and the reaction rate is changed from 0 to 5000 s^{-1}. Again the simulation results show good agreement with the analytical solutions, which further validates the accuracy and feasibility of concentration distribution function reconstruction operator and the CFVLBM computational procedure proposed in this study.

4.2. Natural convection in a square cavity caused by concentration gradient

Similar to temperature gradient, concentration gradient in a square cavity also can cause buoyancy flows [38–40]. In fact, dou-

ble-diffusive problem, namely buoyancy flow induced by combined temperature and concentration gradients has been widely studied [41–43]. In this section, natural convection in a square cavity caused by concentration gradient only is simulated using the CFVLBM.

The physical model for the problem under consideration is shown in Fig. 4. The cavity has an aspect ratio of unity and is filled with an incompressible perfect mixture of a binary fluid that operates in the laminar regime under steady state condition. The Schmidt number Sc ($Sc = v/D$) is fixed as 0.71. The concentration Y_h and Y_c are uniformly imposed along the left wall and right wall respectively. The top and bottom surfaces are assumed to be impermeable. Fluid properties are defined as density $\rho = 1.0$ kg m^{-3}, kinetic viscosity $v = 1.3 \times 10^{-5}$ m^{2}s^{-1}. The computations are conducted for three solutal Rayleigh numbers Ra ($Ra = g\beta\Delta YH^3/Dv = 10^3$, 10^4 and 10^5) with grid number 601×601. The results of CFVLBM simulation are compared carefully with the results using commercial software FLUENT.

The well known Boussinesq approximation [44] is used in the simulation. In Boussinesq approximation, it is assumed that all fluid properties (density, viscosity, thermal diffusivity) can be
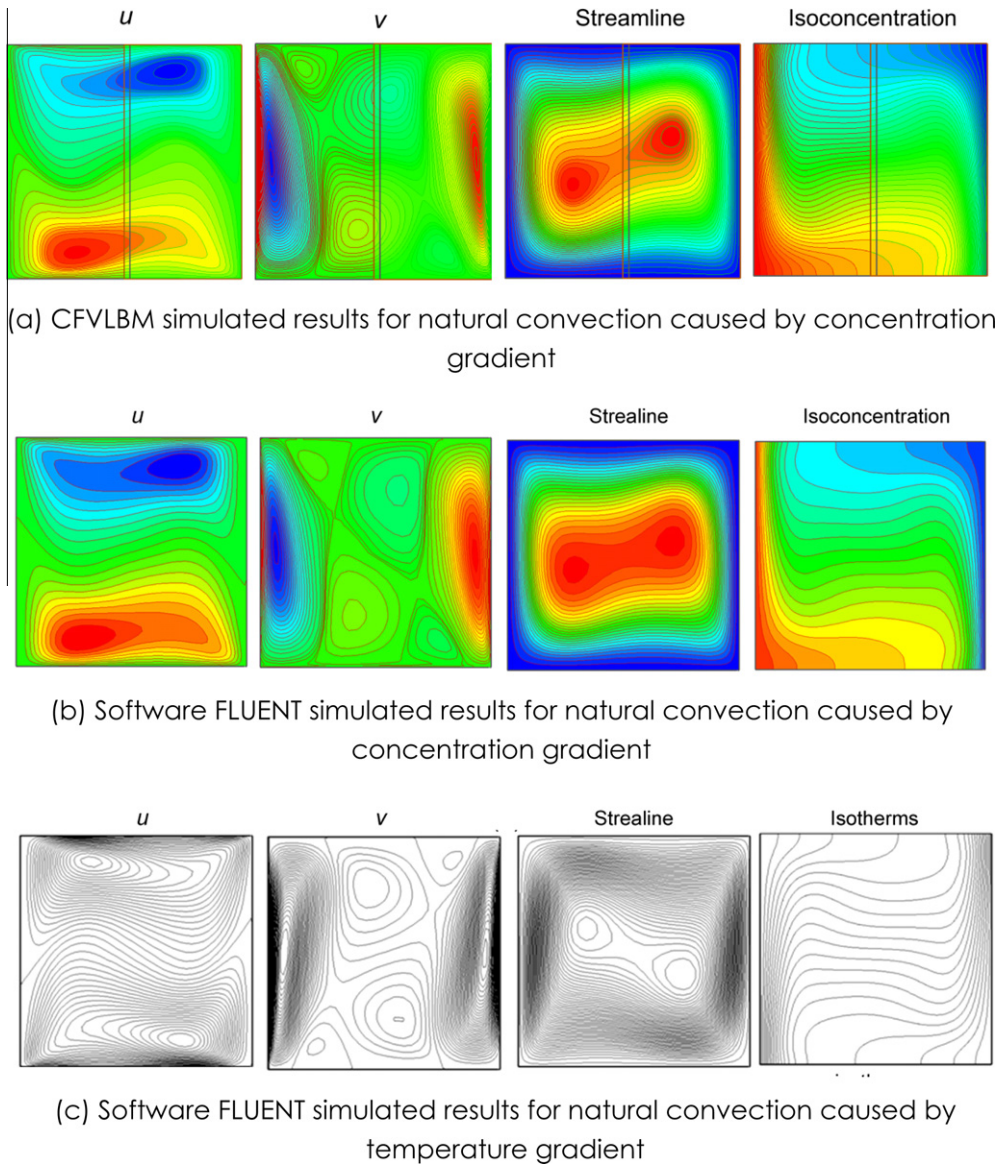
(a) CFVLBM simulated results for natural convection caused by concentration gradient

(b) Software FLUENT simulated results for natural convection caused by concentration gradient

(c) Software FLUENT simulated results for natural convection caused by temperature gradient

Fig. 7. Contour lines for natural convection in square cavity for $Sc = 0.71$ ($Pr = 0.71$) and solutal $Ra = 10^5$ (thermal $Ra = 10^5$).

considered as constant except the density ρ in the body force term, where it is assumed to be a linear function of the concentration

$$\rho = \rho_0[1 + \beta(Y - Y_c)] \tag{54}$$

where ρ_0 are the reference fluid density, β is the coefficient of solutal expansion. With the Boussinesq approximation, the gravity is rewritten as

$$\boldsymbol{G} = \rho_0\boldsymbol{g} + \rho_0\boldsymbol{g}\beta(Y - Y_c) \tag{55}$$

where $\boldsymbol{g}$ is the acceleration of vector of gravity.

The natural convection adopted Boussinesq approximation can be simulated by adding an external force term F_i to the right-hand-side of the evolution Eq. (1) [45]. F_i is defined as

$$F_i = \omega_i\rho\left(1 - \frac{1}{2\tau}\right)\left[\frac{3}{c^2}(\boldsymbol{c}_i \cdot \boldsymbol{F}) + \frac{9}{c^4}(\boldsymbol{c}_i \cdot \boldsymbol{F})^2 - \frac{3}{c^2}\boldsymbol{F}^2\right] \tag{56}$$

where $\boldsymbol{F} = \boldsymbol{g}\beta(Y - Y_c)$.

Fig. 5(a) shows the contour lines of u velocity, v velocity, streamline and isoconcentration for Ra as 10^3 using CFVLBM, while Fig. 5(b) is the corresponding results using FLUENT. It can be seen

that the simulations results of CFVLBM and FLUENT are in good agreement with each other. It is worth mentioning that the concentration gradient induces natural convection in the opposite direction compared with that from temperature gradient. That is, the buoyancy flow induced by concentration gradient is anti-clockwise (high concentration and low concentration are at the left and right walls, respectively), while that induced by temperature gradient is clockwise (i.e., high temperature and low temperature are at the left and right walls, respectively). In fact, if Prandtl number Pr and thermal Rayleigh numbers Ra equal to Sc and solutal Rayleigh numbers Ra respectively, the contour lines of temperature caused natural convection and those of concentration gradient caused one are antisymmetric about the center line of the vertical direction. Fig. 5(c) shows the contour lines of u velocity, v velocity, streamline and isotherms for temperature caused natural convection with Pr of 0.71 and thermal Rayleigh numbers Ra of 10^3. The antisymmetric characteristics can be clearly observed.

Figs. 6(a) and (b) and Figs. 7(a) and (b) shows the contour lines of u velocity, v velocity, streamline and isoconcentration for Ra as 10^4 and 10^5 respectively. Again the simulation results of CFVLBM
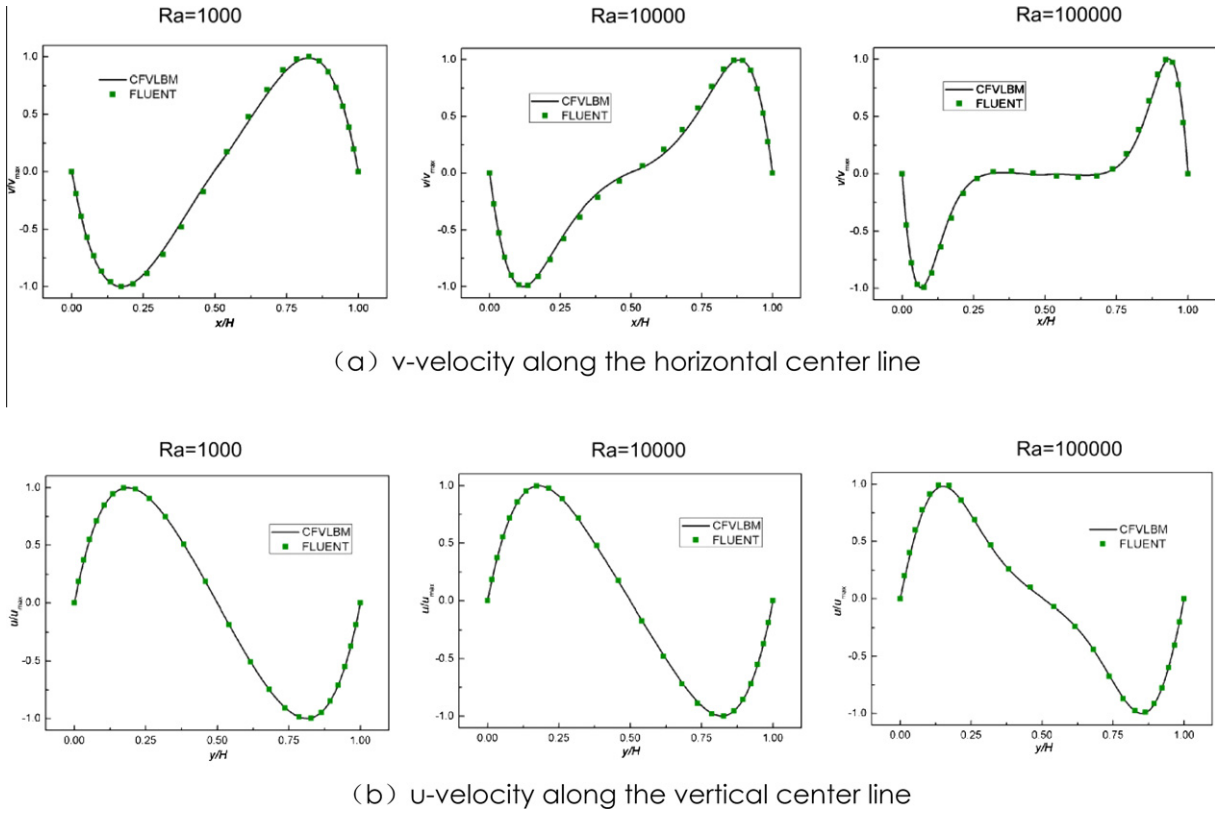
(a) v-velocity along the horizontal center line

(b) u-velocity along the vertical center line

Fig. 8. Comparison between velocities from CFVLBM and FLUENT.
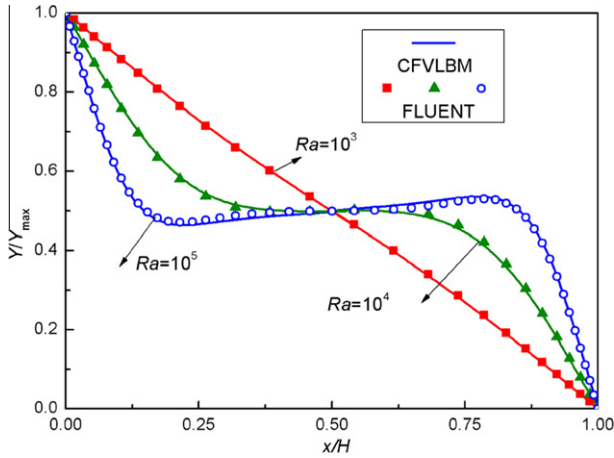

Fig. 9. Comparisons of concentration profiles along the horizontal central line.

and FLUENT agree well with each other. Fig. 6(c) Fig. 7(c) shows the corresponding contour lines for temperature caused natural convection, and the antisymmetric characteristics are perfect.

To further validate the accuracy of CFVLBM, v-velocity along the horizontal center line and u-velocity along the vertical center line are compared with results from FLUENT in Fig. 8, where velocity u is normalized by maximum velocity u_{max} on the vertical center line and v is normalized by the maximum velocity v_{max} on the horizontal center line. It can be observed in Fig. 8 that the predicted results from CFVLBM are consistent with that from FLUENT.

The variation of non-dimensional concentration along the horizontal centerline is shown in Fig. 9. It can be clearly seen that the results of CFVLBM and FLUENT agree well with each other. At $Ra = 10^3$, the concentration drops linearly due to the dominant diffusion mechanism. As Ra increases, the concentration gradients near the two vertical walls increase and the center part becomes flat.

Finally, local and average Sherwood number Sh (dimensionless mass flux) is calculated for the left wall

$$Sh = -\frac{H}{\Delta Y}\left(\frac{\partial Y}{\partial x}\right)_w \tag{57}$$

$$Sh_m = \int_0^H Sh \, dy \tag{58}$$

Table 1
CFVLBM solutions for different solutal Ra (The corresponding values for different thermal Ra are also presented for comparison [46]).

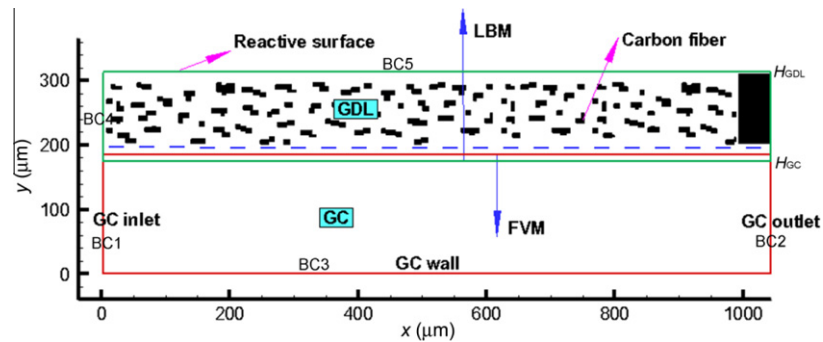| Parameters Sh for concentration, Nu for temperature	$Ra = 10^3$		$Ra = 10^4$		$Ra = 10^5$	
	Concentration	Temperature	Concentration	Temperature	Concentration	Temperature
Sh_m or Nu_m	1.098	1.114	2.190	2.245	4.511	4.510
Sh_{max} or Nu_{max}	1.498	1.581	3.364	3.539	7.629	7.637
$(y/H)_{max}$	0.910	0.099	0.86	0.143	0.915	0.915
Sh_{min} or Nu_{min}	0.659	0.670	0.574	0.583	0.768	0.773
$(y/H)_{min}$	0.005	0.994	0.005	0.994	0.0025	0.999

Fig. 10. Computational domain including a GC and a porous GDL in a PEMFC.

Table 2
Physical parameters.

Quantity	Value
Dimensions of the computational domain	
Length of GC, L	1040 μm
Height of the GC, H_{GC}	200 μm
Height of the GDL, H_{GDL}	120 μm
Porosity of GDL, ε	0.72
Operating conditions	
Pressure of the operation condition, P	1.0×101325 Pa
Temperature of the operation condition, T	343 K
Universal gas constant, R	8.314 J mol^{-1} K^{-1}
Faraday's constant, F	96487°C mol^{-1}
Air inlet velocity, u	1.5 m s^{-1}
Inlet mole fraction rate of oxygen, $X_{O,in}$	0.21
Inlet mole fraction rate of nitrogen, $X_{N,in}$	0.79
Inlet mole fraction rate of water vapor, $X_{w,in}$	0.0
Diffusivity of oxygen in air, D_O	2.84×10^{-5} m^2 s^{-1}
Diffusivity of water vapor in air, D_H	3.55×10^{-5} m^2 s^{-1}
Cathode transfer coefficient, α	1.0
ORR reduction order, γ_c	1
Cathode volumetric reference exchange current density/reference oxygen concentration, $A_t j_{ref}/(C_{O,ref})^{rc}$	120 A mol^{-1} (assumed)

Table 1 lists the maximum Sh_{max} and location of Sh_{max}, minimum Sh_{max} and location of Sh_{min}, and Sh_m. The corresponding values on the hot wall in the natural convection induced by temperature gradient also are presented for comparison [46]. It is expected that *Nusselt* number Nu (maximum, minimum and average values) equals to Sh (maximum, minimum and average values) if $Pr = Sc$ and thermal Rayleigh numbers Ra equals to solutal Rayleigh numbers Ra, and this is the case as can be seen in Table 1. In addition, the locations of Sh_{max} and Sh_{min} reverse along the y axis compared with those of Nu_{max} and Nu_{min}, leading to the sum of the locations of Nu (maximum or minimum) and Sh (maximum or minimum) always equals 1, as shown in Table 1. For example, the location $(y/H)_{max}$ of Sh_{max} for solutal $Ra = 10^3$ is 0.910 and that of Nu_{max} for thermal $Ra = 10^3$ is 0.099, the sum of which is approximately equal to 1.

Simulation results in Section 4 show that the concentration distribution function reconstruction operator and the computational procedure CFVLBM are reliable and accurate to predict the proper phenomenon of fluid flow and mass transport. Thus, we go on further to apply the CFVLBM to simulate multiscale fluid flow and mass transport processes in a PEMFC.

5. Application

In PEMFC, reactants transport from the macro GC through the porous GDL and finally reach the reactive sites. At the reactive
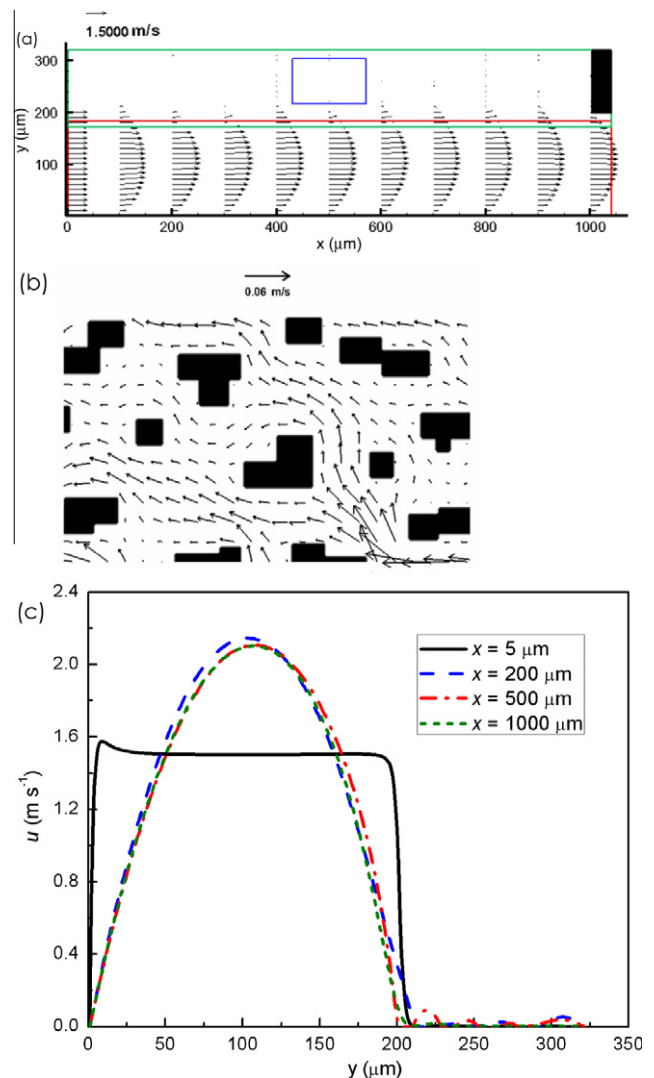

Fig. 11. Velocity distribution. (a) In the GC and GDL, (b) In the local porous GDL marked in the blue rectangles in Fig. 11(a), (c) Velocity profiles along the flow direction (*x* direction). (For interpretation of the references to colour in this figure legend, the reader is referred to the web version of this article.)

sites, electrochemical reaction occurs which consumes oxygen and generates water vapor. The generated water vapor then diffuses through the porous GDL and is finally removed out of the GC. In this section, the CFVLBM is used to simulate the above fluid flow and species transport process. Fig. 10 shows the computational domain consisted of a GC and a porous GDL
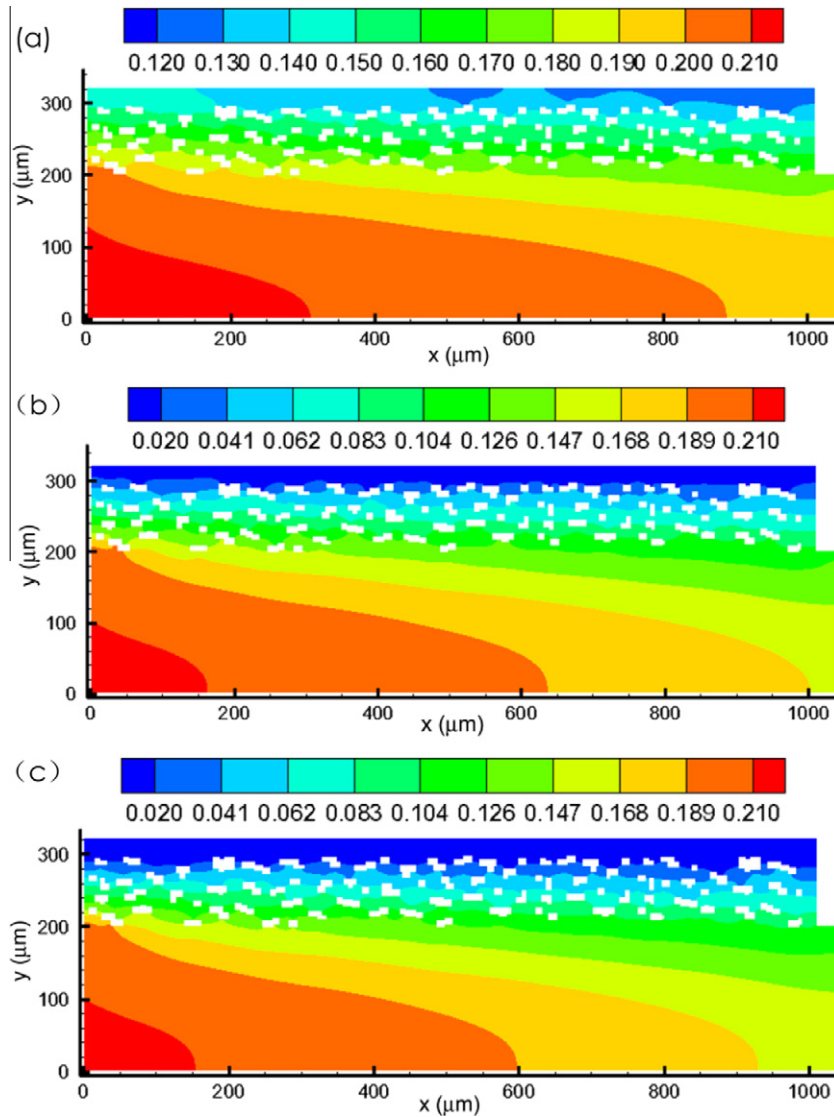
Fig. 12. Oxygen mole fraction distribution for different over-potentials. (a) 0.4 V, (b) 0.5 V, (c) 0.7 V.

(separated by the dashed line). In the porous GDL, irregular rectangles are distributed to simply describe the complex porous structures of GDL.

FVM and LBM are used to simulate fluid flow and mass transport in GC and GDL respectively, as shown in Fig. 10. Three distribution functions in LBM are solved including the density distribution function f_i for flow, $g_{i,o}$ for oxygen transport and $g_{i,w}$ for water vapor transport.

The boundary conditions are as follows. At the GC inlet (BC1), air velocity and species concentration fraction are given:

$$u = u_{in}, \quad v = 0, \quad Y_o = 0.23, \quad Y_n = 0.77, \quad Y_w = 0 \quad (59)$$

where the subscripts o, n and w represent oxygen, nitrogen and water vapor respectively. In the simulation, only the concentrations of oxygen and water vapor are simulated. Concentration of the nitrogen can be obtained by subtracting total concentration to oxygen concentration and water vapor concentration.

At the GC outlet (BC2), GC is extended 40 μm and fully-developed boundary condition is adopted:

$$\frac{\partial u}{\partial x} = 0, \quad \frac{\partial v}{\partial x} = 0, \quad \frac{\partial Y_o}{\partial x} = 0, \quad \frac{\partial Y_n}{\partial x} = 0, \quad \frac{\partial Y_w}{\partial x} = 0 \quad (60)$$

On all the solid walls in the computational domain (BC3, BC4 and solid surfaces of the carbon fibers)

$$u = 0, \quad v = 0, \quad \frac{\partial Y_o}{\partial x} = 0, \quad \frac{\partial Y_n}{\partial x} = 0, \quad \frac{\partial Y_w}{\partial x} = 0 \quad (61)$$

On the top surface (the reactive surface, BC5)

$$u = 0, \quad v = 0, \quad \frac{\partial Y_n}{\partial n} = 0, \quad D_o \frac{\partial Y_o}{\partial n} = -\frac{J}{4F}, \quad D_w \frac{\partial Y_w}{\partial n} = \frac{J}{2F} \quad (62)$$

where F is the Faraday constant. J is the cathode transfer current density and is calculated by [47]

$$J = J_{ref} \left(\frac{Y_o}{Y_{o,ref}} \right) \exp\left(-\frac{\alpha F}{RT} \eta \right) \quad (63)$$

where J_{ref} is the reference exchange current density, α is the transfer coefficient and R is the gas constant. η is the local surface over-potential. Different η specified leads to different mass flux on the reactive surface (BC5). Table 2 lists the physical parameters used in the simulations. It is worth mentioning that flow and mass transport empirical relations in the GDL including empirical relations for permeability and effective diffusivity, which are widely used in
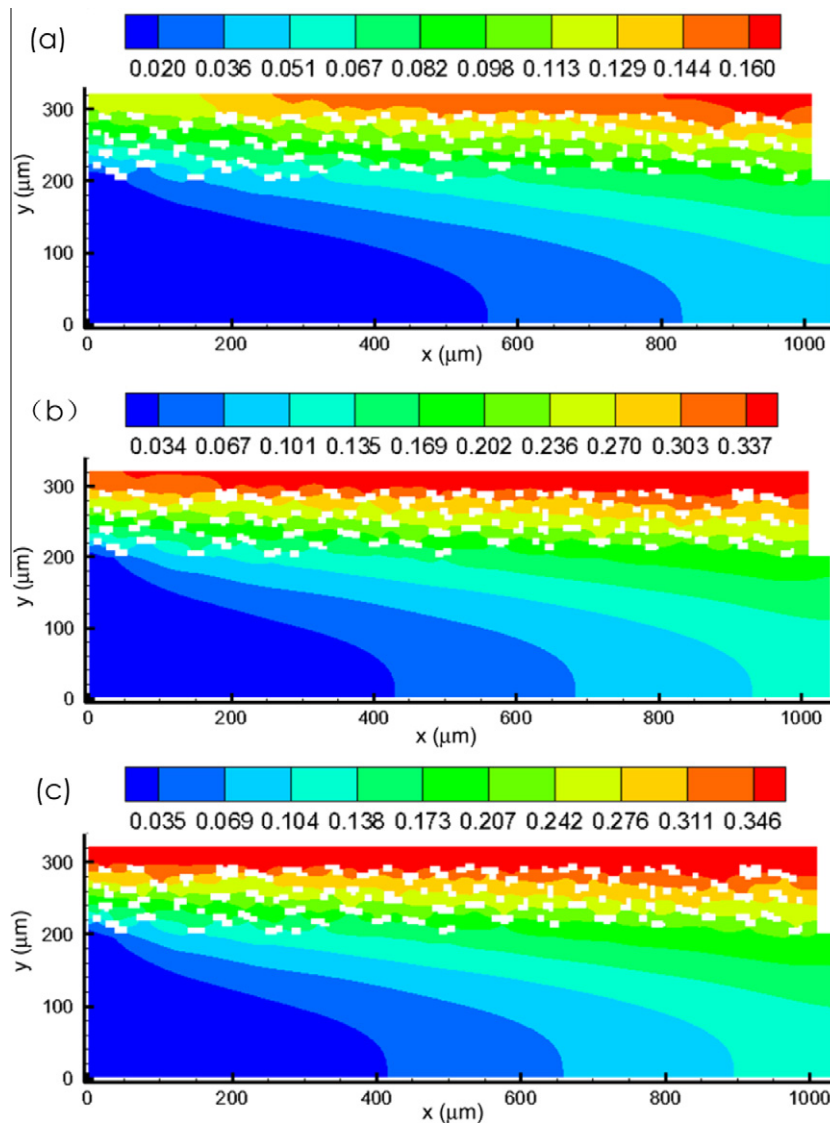
Fig. 13. Water vapor mole fraction distribution for different over-potentials. (a) 0.4 V, (b) 0.5 V, (c) 0.7 V.

macroscopic simulations based on continuum models of PEMFC [47–50], are completely discarded in the present simulation.

Fig. 11(a) shows the velocity vectors obtained from the simulation using CFVLBM. Due to the blockage of the solid rectangles in the GDL, air mainly flows in the GC and magnitude of velocity in the GC is significantly greater than that in the GDL. Fig. 11(b) displays the local detailed velocity vectors in the blue rectangle in Fig. 11(a). It can be seen that fluid flow in the GDL is very complicated due to the complex porous structures of the GDL. Fig. 11(c) further shows the velocity distribution along the flow direction (x direction). It can be seen that velocity profile shows a parabolic shape in the GC and velocity in GDL is extremely low.

Fig. 12 shows the oxygen fraction distribution for over-potential in Eq. (63) as 0.4, 0.5 and 0.7 V, respectively. In each image, the oxygen concentration gradually decreases along flow direction as oxygen is consumed on the reactive surface. High over-potential creates high reaction rate at the reactive site. Thus, as over-potential increases, more oxygen is consumed and oxygen concentration decreases in the computational domain, as shown in Fig. 12. In Fig. 12(c), oxygen concentration near the reactive surface approaches zero, implying that oxygen starvation occurs under the high over-potential which leads to concentration polarization.

Fig. 13 shows the water vapor fraction distribution for over-potential in Eq. (63) as 0.4, 0.5 and 0.7 V, respectively. In each image, the water vapor concentration gradually increases along the flow direction as water vapor is generated on the reactive surface. As the over-potential increases, more water vapor is generated and water vapor concentration in the GC and GDL goes up.

Recently, an increasing number of numerical studies tend to investigate the microscopic and mesoscopic fluid flow and mass transport in PEMFC using LBM [51–56]. LBM is indeed a useful tool for revealing pore-scale flow dynamics because it can simulate based on the real microstructures of porous components in PEMFC including GDL and CL. Unfortunately, LBM surfers the disadvantage of requiring extremely high computational resources as can be found in [51–56]. On the contrary, macroscopic simulations of fluid flow and mass transport in PEMFC based on continuum models [47–50], while with the advantage of numerical efficiency, suffer the disadvantage of neglecting the influence of actual structures and related heterogeneous characteristics of GDL. Due to this neglect, macroscopic continuum models have to employ many flow empirical relations. The accuracy of some of these empirical relations applied to porous components in PEMFC is questionable and needs further validation, as they sometimes predicted

unreasonable distributions in GDL [57]. Fortunately, the coupling modeling strategy can avoid disadvantages of the microscopic, mesoscopic simulation and macroscopic simulation, and can take the advantages of each side [3]. Simulation results in the present study show that CFVLBM can efficiently capture the pore-scale information of fluid flow and mass transport in GDL without using empirical relations and excessive computational resources.

6. Conclusion

In this study, a concentration distribution function reconstruction operator is derived to lift macro concentration to concentration distribution function in LBM. Combined with the density–velocity reconstruction operator developed previously by the authors' group [15], a coupling FVM and LBM modeling computational scheme (CFVLBM) previously proposed in [7] is extended to solve fluid flow and mass transport phenomenon. Diffusion–convection–reaction problem and natural convection in a square cavity induced by concentration gradient are simulated by the CFVLBM. The simulation results validate the feasibility and reliability of the developed concentration reconstruction operator and the CFVLBM scheme.

The CFVLBM is applied to simulate fluid flow and mass transport in the cathode side of a PEMFC. It is found that the CFVLBM can capture the pore-scale information of fluid flow and species transport in the GDL without using the flow empirical relations. In addition, the CFVLBM can save the computational resources compared with that with pure LBM.

The 3D extension of CFVLBM is underway by the authors' group and will be further applied to simulate fluid flow and mass transport in PEMFC and pollutant transport in cities.

Acknowledgment

References

[1] E. Weinan, Multiscale modeling and computation, Notices Am. Math. Soc. 50 (2005) 1062–1070.
[2] W.Q. Tao, Y.L. He, Recent advances in multiscale simulation of heat transfer and fluid flow problems, Prog. Comput. Fluid Dyn. 9 (2009) 150–157.
[3] Y.L. He, W.Q. Tao, Multiscale simualtions of heat transfer and fluid flow problems, ASME J. Heat Transfer 134 (2012) 031018. 13p..
[4] A. Christensen, S. Graham, Multiscale lattice Boltzmann modeling of proton transport in crystalline semiconductor materials, Numer. Heat Transfer B. Fund. 57 (2010) 89–109.
[5] Q.H. Nie, Y. Joshi, Multiscale thermal modeling methodology for thermoelectrically cooled electronic cabinets, Numer. Heat Transfer A. Appl. 53 (2008) 225–248.
[6] E. Samadiani, Y. Joshi, Multi-parameter model reduction in multi-scale convective systems, Int. J. Heat Mass Transfer 53 (2010) 2193–2205.
[7] H.B. Luan, H. Xu, L. Chen, D.L. Sun, W.Q. Tao, Numerical illustrations of the coupling between the lattice Boltzmann method and Finite-Type macro-numerical methods, Numer. Heat Transfer B. Fund. 57 (2010) 147–171.
[8] P. Moin, K. Mahesh, Direct numerical simulation: a tool in turbulence research, Annu. Rev. Fluid Mech. 30 (1998) 539–578.
[9] M. Bubak, G. van Albada, P. Sloot, J. Dongarra, P. Albuquerque, D. Alemani, B. Chopard, P. Leone, Coupling a lattice Boltzmann and a finite difference scheme, in: Computational Science – ICCS 2004, Springer, Berlin, Heidelberg, 2004, pp. 540–547.
[10] B. Mondal, S.C. Mishra, Lattice Boltzmann method applied to the solution of the energy equations of the transient conduction and radiation problems on non-uniform lattices, Int. J. Heat Mass Transfer 51 (2008) 68–82.
[11] J.S. Wu, Y.Y. Lian, G. Cheng, R.P. Koomullil, K.C. Tseng, Development and verification of a coupled DSMC-NS scheme using unstructured mesh, J. Comput. Phys. 219 (2006) 579–607.
[12] X.B. Nie, S.Y. Chen, W.N. E, M.O. Robbins, A continuum and molecular dynamics hybrid method for micro- and nano-fluid flow, J. Fluid Mech. 500 (2004) 55–64.
[13] J. Sun, Y.L. He, W.Q. Tao, Scale effect on flow and thermal boundaries in micro-nano-channel flow using molecular dynamics-continuum hybrid simulation method, Int. J. Numer. Methods Eng. 81 (2010) 207–228.
[14] A. Dupuis, E.M. Kotsalis, P. Koumoutsakos, Coupling lattice Boltzmann and molecular dynamics models for dense fluids, Phys. Rev. E 75 (2007) 046704.
[15] H. Xu, H.B. Luan, Y.-L. He, W.-Q. Tao, A lifting relation from macroscopic variables to mesoscopic variables in lattice Boltzmann method: derivation, numerical assessments and coupling computations validation, Comput. Fluids 54 (2012) 92–104.
[16] S.Y. Chen, G.D. Doolen, Lattice Boltzmann method for fluid flows, Annu. Rev. Fluid Mech. 30 (1998) 329–364, doi:10.1146/annurev.fluid.30.1.329.
[17] H.B. Luan, H. Xu, L. Chen, D.L. Sun, Y.L. He, W.Q. Tao, Evaluation of the coupling scheme of FVM and LBM for fluid flows around complex geometries, Int. J. Heat Mass Transfer 54 (2011) 1975–1985.
[18] Luan HB, Chen L, Feng Y L, He Y L, Tao WQ. Coupling between finite volume method and thermal lattice Boltzmann method and its application to natural convection in a square cavity. Int. J. Numer. Methods Fluids, in press.
[19] Y.L. He, Y. Wang, Q. Li, Lattice Boltzmann Method: Theory and Applications, Science Press, Beijing, China, 2009.
[20] Z. Dong, W. Li, Y. Song, Lattice Boltzmann simulation of growth and deformation for a rising vapor bubble through superheated liquid, Numer. Heat Transfer A. Appl. 55 (2009) 381–400.
[21] S.-K. Choi, C.-L. Lin, A simple finite-volume formulation of the lattice Boltzmann method for laminar and turbulent flows, Numer. Heat Transfer B. Fund. 58 (2010) 242–261.
[22] D. Chatterjee, Lattice Boltzmann simulation of incompressible transport phenomena in macroscopic solidification processes, Numer. Heat Transfer B. Fund. 58 (2010) 55–72.
[23] P.L. Bhatnagar, E.P. Gross, M. Krook, A Model for collision processes in gases. I. Small amplitude processes in charged and neutral one-component systems, Phys. Rev. A 94 (1954) 511–525.
[24] X. He, L.S. Luo, Theory of the lattice Boltzmann equation: from Boltzmann equation to lattice Boltzmann equation, Phys. Rev. E 56 (1997) 6811–6817.
[25] Y.H. Qian, D. d'Humiéres, P. Lallemand, Lattice BGK models for Navier Stokes equation, Europhys. Lett. 15 (1991) 603–607.
[26] S.P. Dawson, S. Chen, G.D. Doolen, Lattice Boltzmann computations for reaction–diffusion equations, J. Chem. Phys. 98 (1993) 1514–1523.
[27] S.P. Sullivan, F.M. Sani, M.L. Johns, L.F. Gladden, Simulation of packed bed reactors using lattice Boltzmann methods, Chem. Eng. Sci. 60 (2005) 3405–3418.
[28] S.V. Patankar, A calculation procedure for two-dimensional elliptic situation, Numer. Heat Transfer 4 (1981) 409–425.
[29] J.P.V. Doormaal, G.D. Raithby, Enhancement of the SIMPLE method for predicting incompressible fluid flow, Numer. Heat Transfer 7 (1984) 147–163.
[30] R.I. Issa, Solution of the implicit discretized fluid-flow equations by operator splitting, J. Comput. Phys. 62 (1986) 40–65.
[31] R.H. Yen, C.H. Liu, Enhancement of the SIMPLE algorithm by an additional explicit correction step, Numer. Heat Transfer B 24 (1993) 127–141.
[32] B. Yu, H. Ozoe, W.Q. Tao, A modified pressure-correction scheme for the SIMPLER method, MSIMPLER, Numer. Heat Transfer B. Fund. 39 (2001) 435–449.
[33] W.Q. Tao, Z.G. Qu, Y.L. He, A novel segregated algorithm for incompressible fluid flow and heat transferproblems – Clear (coupled and linked equations algorithm revised), part I: mathematical formulation and solution procedure, Numer. Heat Transfer B. Fund. 45 (2004) 1–17.
[34] W.Q. Tao, Z.G. Qu, Y.L. He, A novel segregated algorithm for incompressible fluid flow and heat transferproblems – Clear (coupled and linked equations algorithm revised), part I: mathematical formulation and solution procedure: application examples, Numer. Heat Transfer B. Fund. 45 (2004) 19–48.
[35] D.L. Sun, Z.G. Qu, Y.L. He, W.Q. Tao, An ef?cient segregated algorithm for incompressible fluid flow and heat transfer problems – IDEAL (inner doubly iterative efficient algorithm for linked equations), part I: mathematical formulation and solution procedure, Numer. Heat Transfer B. Fund. 53 (2008) 1–17.
[36] D.L. Sun, Z.G. Qu, Y.L. He, W.Q. Tao, An ef?cient segregated algorithm for incompressible fluid flow and heat transfer problems – IDEAL (inner doubly iterative efficient algorithm for linked equations), part II: application examples, Numer. Heat Transfer B. Fund. 53 (2008) 18–38.
[37] Z.Y. Li, W.Q. Tao, A new stability-guaranteed second-order difference scheme, Numer. Heat Transfer B. Fund. 42 (2002) 349–365.
[38] G.D.V. Davis, Natural convection of air in a square cavity: a benchmark numerical solution, Int. J. Numer. Methods Fluids 3 (1983) 249–264.
[39] T. Saitoh, K. Hirose, High-accuracy bench mark solutions to natural convection in a square cavity, Comput. Mech. 4 (1989) 417–427.
[40] B. Gebharta, L. Peraa, The nature of vertical natural convection flows resulting from the combined buoyancy effects of thermal and mass diffusion, Int. J. Heat Mass Transfer 14 (1971) 2025–2050.
[41] V.A.F. Costa, Double diffusive natural convection in a square enclosure with heat and mass diffusive walls, Int. J. Heat Mass Transfer 40 (1997) 4061–4071.
[42] A.J. Chamkha, H. Al-Naser, Hydromagnetic double-diffusive convection in a rectangular enclosure with opposing temperature and concentration gradients, Int. J. Heat Mass Transfer 45 (2002) 2465–2483.
[43] M.A. Teamah, W.M. El-Maghlany, Numerical simulation of double-diffusive mixed convective flow in rectangular enclosure with insulated moving lid, Int. J. Therm. Sci. 49 (2010) 1625–1638.
[44] D.D. Gray, A. Giorgin, The validity of the Boussinesq approximation for liquids and gases, Int. J. Heat Mass Transfer 19 (1976) 545–551.

[45] Z.L. Guo, T.S. Zhao, Lattice Boltzmann model for incompressible flows through porous media, Phys. Rev. E 66 (2002). 036304.036301–036304.036309.

[46] G. Barakos, E. Mitsoulis, Natural convection flow in a square cavity revisited: laminar and turbulent models with wall function, Int. J. Numer. Methods Eng. 18 (1994) 695–719.

[47] A.D. Le, B. Zhou, A general model of proton exchange membrane fuel cell, J. Power Sources 182 (2008) 197–222.

[48] Z.H. Wang, C.Y. Wang, K.S. Chen, Two-phase flow and transport in the air cathode of proton exchange membrane fuel cells, J. Power Sources 94 (2001) 40–50, doi:10.1016/S0378-7753(00)00662-5.

[49] L. You, H. Liu, A two-phase flow and transport model for the cathode of PEM fuel cells, Int. J. Heat Mass Transfer 45 (2002) 2277–2287, doi:10.1016/S0017-9310(01)00322-2.

[50] T. Berning, N. Djilali, A 3D, multiphase, multicomponent model of the cathode and anode of a PEM Fuel cell, J. Electrochem. Soc. 150 (2003) A1589–A1598.

[51] J. Park, M. Matsubara, X. Li, Application of lattice Boltzmann method to a micro-scale flow simulation in the porous electrode of a PEM fuel cell, J. Power Sources 173 (2007) 404–414, doi:10.1016/j.jpowsour.2007.04.021.

[52] J. Park, X. Li, Multi-phase micro-scale flow simulation in the electrodes of a PEM fuel cell by lattice Boltzmann method, J. Power Sources 178 (2008) 248–257, doi:10.1016/j.jpowsour.2007.12.008.

[53] P.P. Mukherjee, C.Y. Wang, Q. Kang, Mesoscopic modeling of two-phase behavior and flooding phenomena in polymer electrolyte fuel cells, Electrochim. Acta 54 (2009) 6861–6875.

[54] L. Hao, P. Cheng, Lattice Boltzmann simulations of anisotropic permeabilities in carbon paper gas diffusion layers, J. Power Sources 186 (2009) 104–114, doi:10.1016/j.jpowsour.2008.09.086.

[55] L. Hao, P. Cheng, Lattice Boltzmann simulations of water transport in gas diffusion layer of a polymer electrolyte membrane fuel cell, J. Power Sources 195 (2010) 3870–3881.

[56] L. Chen, H.-B. Luan, Y.-L. He, W.-Q. Tao, Pore-scale flow and mass transport in gas diffusion layer of proton exchange membrane fuel cell with interdigitated flow fields, Int. J. Therm. Sci. 51 (2012) 132–144.

[57] K.J. Lee, J.H. Nam, C.J. Kim, Pore-network analysis of two-phase water transport in gas diffusion layers of polymer electrolyte membrane fuel cells, Electrochim. Acta 54 (2009) 1166–1176, doi:10.1016/j.electacta.2008.08.068.